Scanning laser triangulation sensor geometry maintaining imaging condition

Johannes Schlarp * **Ernst Csencsics** * **Georg Schitter** *

* *Christian Doppler Laboratory for Precision Engineering for Automated In-Line Metrology, Automation and Control Institute (ACIN), TU Wien, Vienna A-1040, Austria (e-mail: schlarp@acin.tuwien.ac.at).*

Abstract: This work deals with the system design, control and the experimental results of a scanning laser sensor in which the optical path is scanned by a novel high performance compact fast steering mirror (FSM). The system design satisfies the Scheimpflug condition even though only the illumination path is scanned, such that an FSM with a small aperture size and high bandwidth can be used. To scan the area of interest with the FSM, raster trajectories are employed, which provide an uniform spatial resolution over the scan area. To track the trajectory a feedback controller is designed using the H_∞-approach, such that a closed loop bandwidth of 1.4 kHz is achieved. The FSM can follow triangular signals up to 200 Hz with the maximum actuation range of $\pm 3°$. This enables a framerate of up to two frames per second for an image with 100x100 pixels. With the scanning system a maximum spatial resolution of 60 μm and a scan range of 25 mm can be achieved.

Keywords: Absolute measurement, Precision measurements, 3D Sensor, Laser Sensor, Fast Steering Mirror, Optical Sensing and Sensors, System Design, Scheimpflug Condition

1. INTRODUCTION

A key technology for the production of the future is the in-line metrology [Schmitt and Moenning (2006); Kunzmann et al. (2005)]. This requires fast and high resolution measurement systems, which preferably generate three dimensional (3D) images [Leopold et al. (2003)]. State of the art 3D measurement systems are mechanical scanning systems, like coordinate measurement machines [Pfeifer (2013)]. These systems manipulate the position of the sample or sensor, which can be a tactile probe [Weckenmann et al. (2004)] or an optical point sensor [Schwenke et al. (2002)], with external actuators. As described in [Yu et al. (2017)], the achievable scan speed of such an mechanical scanning system is strongly restrained by the large moving mass. If a higher throughput is required generally camera-based systems, e.g. based on structured light, are used [Leach (2011)]. This optical surface sensors, however, suffer from a limited resolution of about 10 μm [Keferstein and Dutschke (2010)].

In [Schlarp et al. (2018d)] two optical scanning systems which manipulate only the optical path of a line sensor are presented. Since the moving mass of an integrated compact optical scanning system can be significantly smaller as compared to external mechanical scanning systems, higher scan speeds can be achieved, without impairing the lateral resolution of the measurement system [Schlarp et al. (2018c)]. Due to their high resolution of down to 30 nm and their large measurement range of up to 1 m, triangulation sensors are one of the most commonly used optical sensors for quality control tasks [Brosed et al. (2010)]. The main components of these sensors are a laser source, an imaging lens and a detector [Donges and Noll (2015)]. In order to
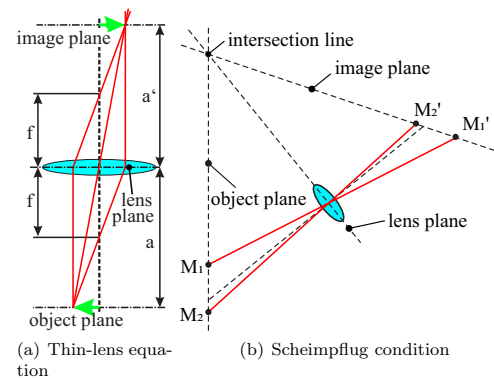

(a) Thin-lens equation

(b) Scheimpflug condition

Fig. 1. Schematic illustration of (a) the thin-lens equation and (b) the Scheimpflug condition, which is a generalized form of the equation for tilted planes.

precisely obtain the distance between sample and sensor, the diffusely scattered laser light spot from the sample must be projected sharply onto the detector [Keferstein and Dutschke (2010)]. To project an object on the object plane correctly onto the image plane, as illustrated in Fig. 1(a), the thin-lens equation must be satisfied, which can be given by

$$\frac{1}{f} = \frac{1}{a} + \frac{1}{a'}, \tag{1}$$

with the focal length of the lens f, the distance between lens and object plane a and the distance between lens and image plane a'. The thin-lens equation is, however, only valid, if all three planes are parallel, which is not

the case for the components of a triangulation sensor. In order to generate a sharp projection, the components of the triangulation sensor are aligned according to the Scheimpflug condition [Blais et al. (1988)], which is a generalized form of the thin-lens equation for non parallel planes. The Scheimpflug condition is fulfilled, if the object, the lens and the image plane intersect in a single line (intersection line), as depicted in Fig. 1(b).

In a recently published design of a scanning triangulation sensor [Schlarp et al. (2018d)] both optical paths of the sensor are manipulated by a fast steering mirror (FSM), such that the basic measurement geometry of the sensor is not affected and the Scheimpflug condition is maintained. Another system design [Schlarp et al. (2018d)] manipulates only the illumination path of the sensor by an FSM, which leads to a violation of the Scheimpflug condition and introduces a related additional measurement error [Schlarp et al. (2018b)]. A benefit of this design is, however, that an FSM with a smaller aperture size can be used, if only the illumination path is scanned, such that even higher scan speeds can be achieved. Furthermore, the FSM can generally be positioned closer to the sensor, such that a larger lateral scan range can be achieved as compared to a scanning system which manipulates both optical paths.

The contribution of this paper is the system design of a scanning triangulation sensor system, which manipulates only the illumination path of the sensor by a compact FSM, while still satisfying the Scheimpflug condition. In Section 2 the system design and the geometrical relations for image reconstruction are presented. The system hardware, controller design and scan trajectories are described in Section 3. The measurement results are discussed in Section 4, while Section 5 concludes the paper.

2. SYSTEM DESIGN AND IMAGE RECONSTRUCTION

2.1 System Design

A laser line sensor (type: LLT 2810-25, Micro-Epsilon GmbH, Germany) with a measurement range of 25 mm and a resolution of 10 μm is selected as the starting point for the system design. From the sensor only the lens set, the detector and the evaluation unit are used. The surface of the sample is illuminated by a laser beam, which is generated from a dot laser module. To change the position of the laser spot on the sample, the orientation of the laser beam is manipulated by means of an FSM. As discussed in Section 1, a sharp projection of the scattered laser spot on the sample onto the detector is necessary, to correctly determine the distance between sensor and sample. For point or line triangulation sensors this can be realized by aligning the object, lens and image plane according to the Scheimpflug condition. For a three dimensional measurement system, however, the position and orientation of the object plane changes during the scanning motion, such that it is difficult to fulfil this imaging condition. By placing the mirror surface of the FSM scanner on the intersection line of the lens and image plane the condition can be satisfied at each measurement point [Schlarp et al. (2019)], since the object plane rotates around the intersection line. For the used laser line sensor,

the intersection line is too close to the circuit board of the evaluation unit, such that the FSM surface cannot be positioned directly on the actual intersection line. By inserting an additional static mirror between the FSM and the sample, as depicted in Fig. 2, the optical path between the static mirror and the laser source can be folded around the surface of the static mirror, such that the FSM is optically placed on the intersection line. Therefore, the distance d_{FSM} between the FSM and static mirror has to be equal to the distance between the static mirror and the intersection line. This distance together with the angular range of the FSM also determines the required aperture size for the static mirror.
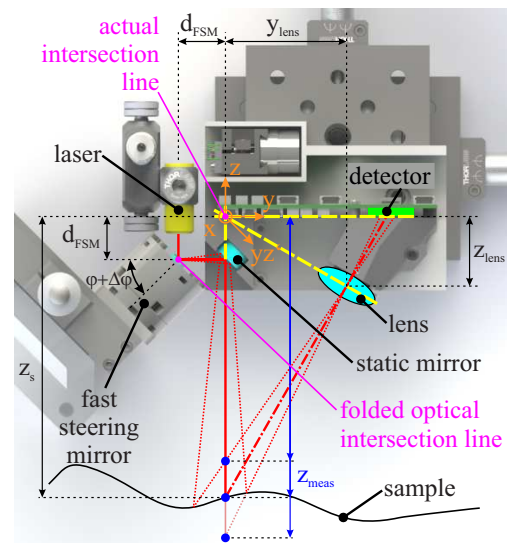

Fig. 2. Schematic setup of the scanning triangulation system with characteristic dimensions. The position of the laser spot on the sample can be manipulated by the FSM. Through the static mirror, the FSM is optically positioned on the intersection line.

To manipulate the illumination path a novel high performance compact FSM is used, which is described in detail in [Csencsics et al. (2018)]. The achievable range times bandwidth product of this hybrid reluctance actuated system is significantly higher as compared to state of the art voice coil actuated FSMs and the system dimensions are as small as $\varnothing 32$ x 30 mm. The orientation of the FSM φ and the static mirror is $45°$ with respect to the xz-plane, to enable good alignment of the system components. The outer diameter of the compact FSM is 32 mm, such that the distance d_{FSM} is selected to 20 mm. At this distance a static mirror (type: PF05-03-P01, Thorlabs Inc., USA) with an aperture size of 12.7 mm is sufficient to redirect the laser beam to the sample over the entire scan range.

2.2 Image Reconstruction

The measured quantities consist of $\Delta\varphi$, $\Delta\vartheta$, which are the angular position of the FSM around the x-, yz'-axis and z_{meas}, which is the reconstructed distance from the distance measured on the detector of the laser line sensor.

As can be observed in Fig. 2, this reconstructed distance z_{meas} is acquired in the xz-plane. To reconstruct the surface profile of the sample from the measured quantities, geometrical relations need to be determined. With the similarity theorems for triangles the distance z_s between sensor and sample in the z-direction and the reconstructed distance z_{meas} can be linked in the following form

$$\frac{z_{meas} - z_{lens}}{y_{lens}} = \frac{z_s - z_{lens}}{y_{lens} - y_s}, \qquad (2)$$

in which y_s is the position of the laser spot on the sample in the y-direction, and y_{lens} and z_{lens} are the position of the lens in the y- and z-direction, respectively. By rearranging this equation and with the use of trigonometric functions the surface profile which is described by x_s, y_s and z_s can be calculated by

$$z_s = \frac{z_{meas} \cdot y_{lens}}{y_{lens} + (z_{meas} - z_{lens}) \cdot \tan(2\Delta\varphi)} \qquad (3a)$$

$$x_s = z_s \cdot \tan(2\Delta\vartheta) \cdot \cos(\varphi + \Delta\varphi) \qquad (3b)$$

$$y_s = z_s \cdot \tan(2\Delta\varphi), \qquad (3c)$$

with $\Delta\varphi$ and $\Delta\vartheta$ the angular position of the FSM around the x- and yz'-axis, respectively. The measurement range z_s of the laser line sensor is between 106 mm and 131 mm. Since the actuation range of the compact FSM is $\pm3°$, the maximum achievable scan range is 19.5 mm and 27.5 mm in x- and y-direction, respectively. The maximum lateral resolution of the scanning system is determined by the laser spot diameter on the sample. The used laser spot size on the sample is 60 μm in the center of the measurement range and expands to 250 μm towards the edges of the measurement range, due to divergence of the Gaussian beam. The resolution in the z-direction is determined by the used laser line sensor to 10 μm.

3. SYSTEM HARDWARE AND SCAN TRAJECTORIES

3.1 Experimental setup

Fig. 3 depicts the experimental setup of the scanning system. In order to align the various components according to the system design, the laser source is mounted on a post assembly and the remaining components are mounted on manual linear stages.
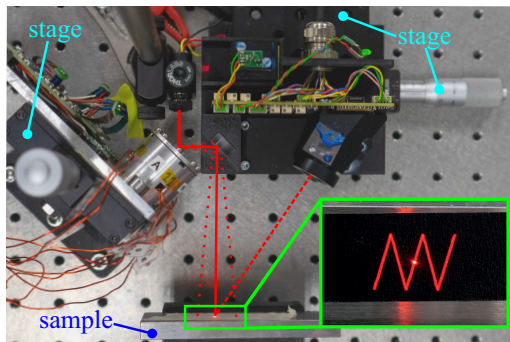

Fig. 3. Experimental setup of the optical scanning system and long time exposure of a low resolution raster scan trajectory.

3.2 Identification

To design tailored feedback controllers for the FSM, a model of each system axis of the FSM is necessary. To derive this model the system dynamics of the two system axis are measured with a system analyzer (type: 3562A, Hewlett-Packard, USA). The current through the coils serve as the system inputs, while the angular positions of the mirror are the system outputs.

Fig. 4 depicts the measured frequency response of the tip (solid red) and tilt axis (solid magenta). Due to manufacturing tolerances the resonance frequency of the tilt axis is higher (415 Hz) as compared to the tip axis (315 Hz), such that separate models for each system axis are derived. Beyond the resonance frequency an increasing phase lag as well as a slope of -50 dB is observable for both system axes. This fractional order slope can be explained by eddy currents in the flux conducting parts of the actuator, which can be modelled by a lag-lead term [Csencsics et al. (2018)]. At about 2 kHz the noise floor ($\sim$ -60 dB) of the system is reached.
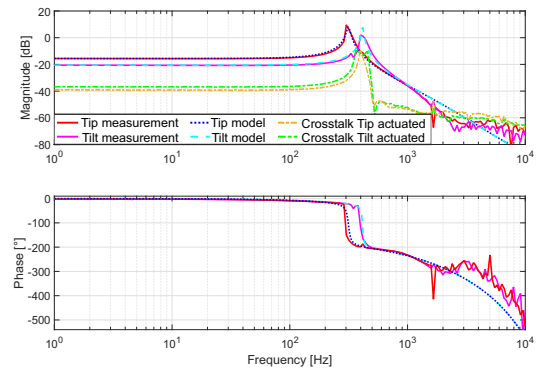

Fig. 4. Measured and modelled frequency response of the tip and tilt axis. The resonance frequencies of the tip and tilt axis are at 315 Hz and 415 Hz, respectively. The measured crosstalks between the two axes are 16 dB lower then the single axis response.

Fig. 4 also shows the magnitude response of the crosstalk frequency responses (dashed dotted green and orange) between the two system axes. Since the magnitudes are about 16 dB lower as compared to the single axis transfer function (TF) over the relevant part of the frequency spectrum, each system axis can be controlled by a single-input-single-output (SISO) controller. The dynamics of each system axis can be modelled by

$$P(s) = K \cdot \underbrace{\frac{\omega_0^2}{s^2 + 2\zeta_0\omega_0 s + \omega_0^2}}_{\text{mass spring damper}} \cdot \overbrace{\frac{s + \omega_1}{s + \omega_2}}^{\text{eddy current}} \cdot \underbrace{e^{s \cdot T_d}}_{\text{time delay}}, \quad (4)$$

with parameters according to Table 1 and DC gains of $K_{Tip} = 0.1663$ and $K_{Tilt} = 0.0935$ of the tip and tilt axis, respectively. A time delay of $T_d = 100\mu s$ is used to model the sensor system. The modelled TFs of the tip (dotted blue) and tilt axis (dashed cyan) are also shown in Fig. 4.

Table 1. Coefficients of the modelled FSM system axes.

Axis	Index	ω_{Index} [rad/s]	ζ_{Index}
Tip	0	1.98e3	0.033
Tilt	0	2.61e3	0.0187
Tip and Tilt	1	6.28e4	-
Tip and Tilt	2	1.26e4	-

3.3 Feedback Control

Based on the identified system dynamics feedback controllers are designed for the tip and tilt axis using an H_∞-approach [Schitter et al. (2004); Kwakernaak (1993)]. The controllers are derived by minimizing the H-norm of the used extended model of a single axis. Fig. 5 depicts this model, which consists out of the controller C, the identified system dynamic P and the weighting functions W_S and W_U for the sensitivity function and input sensitivity function, respectively. Furthermore, the reference mirror position r, the sensed position p, the resulting error e, the control effort u and the measurement noise n are observable in the model.
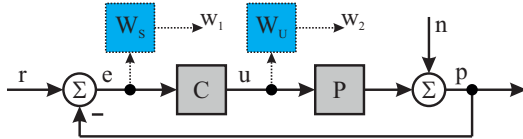

Fig. 5. Block diagram of the extended model for the derivation of a feedback controller for one system axis. The weighting functions W_S and W_U for the sensitivity function and input sensitivity function are used to shape the controller C.

In order to guarantee a sufficient phase margin, the open loop crossover frequency is selected to 700 Hz. To enforce a good tracking within the selected bandwidth the requirements on the sensitivity function is formulated by the weighting function

$$W_S(s) = 0.1 \cdot \frac{s + z_{ws}}{s + p_{ws}}, \quad (5)$$

with the crossover frequency $z_{ws} = 2\pi \cdot 700$ Hz and $p_{ws} = 2\pi \cdot 0.01$ Hz. The weighting function W_S has a tamed inverse high pass behaviour, such that a good tracking at low frequencies is achieved [Csencsics et al. (2017)]. In order to reduce the control effort at high frequencies the weighting function W_U of the input sensitivity function is selected to

$$W_U(s) = 0.0707 \cdot \frac{s + z_{wu}}{s + p_{wu}}, \quad (6)$$

with $z_{wu} = 2\pi \cdot 10$ kHz and $p_{wu} = 2\pi \cdot 100$ MHz. This leads to a low pass behaviour of the resulting system at higher frequencies. With the selected weighting functions and the model of the two system axis, described in Section 3.2, the feedback controller of both axis can be derived to

$$C(s) = V \cdot \frac{\prod\limits_{i=1}^{3} s + \omega_{az_i}}{\prod\limits_{i=1}^{4} s + \omega_{ap_i}} \cdot \frac{\prod\limits_{i=1}^{2} s^2 + 2\zeta_{bz_i}\omega_{bz_i}s + \omega_{bz_i}^2}{\prod\limits_{i=1}^{2} s^2 + 2\zeta_{bp_i}\omega_{bp_i}s + \omega_{bp_i}^2}, \quad (7)$$

with the gain $V = 1.374e7$ and the coefficients according to Table 2 for the tip axis and $V = 1.376e7$ and the parameters according to Table 3 for the tilt axis.

Table 2. Coefficients of the controller for the tip axis.

Index	1	2	3	4
$\omega_{az_{\text{Index}}}$ [rad/s]	1.26e4	1.26e5	6.28e8	-
$\omega_{ap_{\text{Index}}}$ [rad/s]	0.033	6.3e4	4.82e5	9.49e6
$\zeta_{bz_{\text{Index}}}$	0.15	1	-	-
$\omega_{bz_{\text{Index}}}$ [rad/s]	1.98e3	1.26e5	-	-
$\zeta_{bp_{\text{Index}}}$	0.87	0.56	-	-
$\omega_{bp_{\text{Index}}}$ [rad/s]	2.39e4	4.68e5	-	-

The resulting TF of the controller (dotted green) of the tip axis is shown in Fig. 6. For low frequencies a high gain can be observed, such that a zero steady-state error is achieved. For a high phase margin at the selected crossover frequency, the phase of the controller increases between 100 Hz and 1 kHz. The measured open loop frequency response (dashed red) of the tip axis with the implemented controller is also depicted in Fig. 6. The crossover frequency of the system is 642 Hz. At this frequency a phase margin of 40° can be observed, the gain margin of the system is 10 dB. At around 315 Hz a peak in the magnitude response is observable, which matches the resonance frequency of the tip axis. The control effort at this frequency is only slightly reduced by the controller, to ensure a stable system behaviour even if slight parameter changes occur.
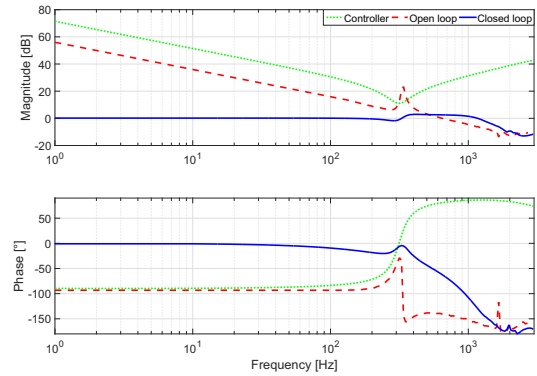

Fig. 6. Measured controller TF (dotted green), loop gain (dashed red) and complementary sensitivity function (solid blue) of the tip axis. The crossover frequency of the open loop system is 642 Hz, with a phase margin of 40°.

Fig. 6 also depicts the measured complementary sensitivity function (solid blue) of the system. Due to the low magnitude of the loop gain at around 300 Hz, the magnitude and phase of the complementary sensitivity function slightly decrease around this frequency. By selecting a higher crossover frequency, the magnitude of the loop gain could be increased, such that this decline could be avoided. Due to the high time delay of the sensor system (100 μs), the crossover frequency can not be increased, without impairing the phase margin. The achieved -3 dB bandwidth of the tip axis is 1.4 kHz, the maximum peaking of 2.9 dB

is reached at 400 Hz. For the tilt axis the same -3 dB bandwidth was achieved, with a slightly higher peaking (3.42 dB).

Table 3. Coefficients of the controller for the tilt axis.

Index	1	2	3	4
$\omega_{az_{\text{Index}}}$ [rad/s]	1.26e4	1.26e5	6.28e8	-
$\omega_{ap_{\text{Index}}}$ [rad/s]	0.032	6.3e4	4.79e5	9.53e6
$\zeta_{bz_{\text{Index}}}$	0.2	1	-	-
$\omega_{bz_{\text{Index}}}$ [rad/s]	2.61e3	1.26e5	-	-
$\zeta_{bp_{\text{Index}}}$	0.88	0.56	-	-
$\omega_{bp_{\text{Index}}}$ [rad/s]	2.39e4	4.63e5	-	-

3.4 Scan Trajectory

Appropriate scan patterns are required to scan the area of interest on the sample. Raster trajectories are applied in various applications, like scanning electron microscopes [Goldstein et al. (2017)], atomic force microscopes [Schitter and Stemmer (2004)] and imaging systems [Ito et al. (2018)]. A raster trajectory is generated by applying a slow triangular signal to one system axis and a fast triangular signal to the other axis. The resulting scan trajectory has a uniform scan speed and spatial resolution [Hedding (1990)], as shown in Fig. 7(a).
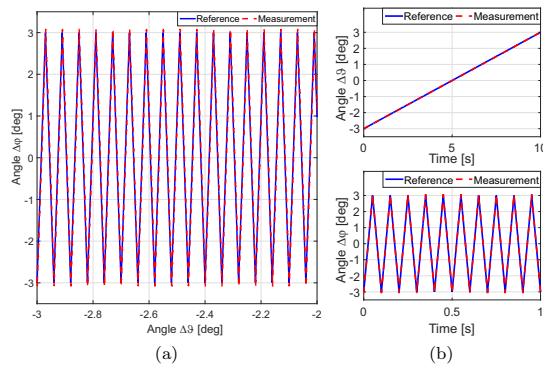

Fig. 7. Raster trajectory. (a) demonstrates the dual axis operation. A raster trajectory with an amplitude of 3° and a frequency of 0.05 Hz for the slow and 10 Hz for fast triangular signal is tracked. (b) depicts the tracking over the time for both axis.

For the optical scanning system an image with 100 x 100 pixels is desired. Since the sample rate of the laser line sensor is 1 kHz, the scan speed of the fast triangular reference signal is selected to 10 Hz. For the slow triangular reference signal only the rising half of the trajectory is used to scan the sample (see Fig. 7(b)), such that the frequency needs to be 200 times smaller as compared to the fast triangular signal. With the chosen frequencies of 100 Hz and 0.05 Hz, a framerate of 0.1 frames per second can be achieved. Fig. 7(a) demonstrates the dual axis operation, with the selected frequencies and an amplitude of 3°. The rms error is $35m°$ and $2.7m°$ for the fast and slow triangular signal, respectively. As can be observed, the framerate is strongly determined by the sample rate of the applied laser line sensor. Since the compact FSM can

be operated with the maximum actuation range of $\pm 3°$ and a triangular signal up until 200 Hz, a framerate of 2 frames per second at a resolution of 100 x 100 pixels would be possible. The actuation range of both axes of the FSM can be selected, such that large area scans as well as high resolution sectional scans can be performed. Large area scans and high resolution scans can also be combined to automatically detect features on the sample and rescan them with a higher resolution [Schlarp et al. (2018a)].

4. VALIDATION OF THE MEASUREMENT RESULTS

To validate the performance of the scanning system the hollow cylinder shaped feature on a Duplo brick (type: Duplo Brick 2 x 4, Lego, Billund, Denmark), which is shown in Fig. 8(a), was measured. Reference measurements of this object were performed in previous experiments with a mechanical scanning system [Schlarp et al. (2018c)], such that the measurement results of the proposed system can be validated. Fig. 8(b) depicts the measured surface profile, which features a similar shape to the in Fig. 8(a) shown sample. Furthermore, the height and thickness of the hollow cylinder appears to be constant. An incorrect value at $x = 5$ mm and $y = 0$ mm can be obtained in the surface profile, which is caused by multiple reflections at the edge of the cylinder. This type of artefact can be handled by inserting a threshold, which determines the valid height of the sample. Along the y-axis the edges of the cylinder do not appear as steeply as along the x-axis. This is caused by shading effects in the optical path of the laser sensor (see Fig. 2), such that certain areas on the sample can not be obtained. To reconstruct the surface profile, the missing measurement points are linear interpolated, which leads to the decreased slope along the y-axis. The height of the hollow cylinder was determined with the reference measurement to 4.663 mm [Schlarp et al. (2018c)]. This dimension was determined with the optical scanning system to 4.577 mm with a standard deviation of 87.7 μm, which matches the result of the reference measurement.

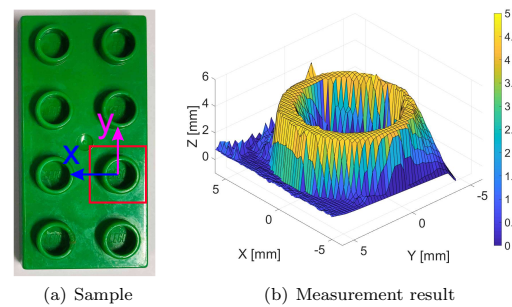
(a) Sample   (b) Measurement result

Fig. 8. Measurement result. (a) shows the sample and selected area of interest. (b) depicts the measured and reconstructed surface profile.

In summary, the feasibility of an optical scanning system, which maintains the Scheimpflug condition even tough only the illumination path of the sensor is scanned with a compact high performance hybrid reluctance actuated fast steering mirror is demonstrated.

5. CONCLUSION

In this paper the design, control and a first measurement result of a scanning laser triangulation sensor, which maintains the imaging condition are shown. To satisfy the Scheimpflug condition at each measurement point, the FSM is placed on the intersection line of the lens and image plane. The optical path between FSM and sample is folded by a static mirror, such that the FSM can be mounted elsewhere and is still optically positioned on the intersection line. With the the geometrical relations, which are determined from the system design, the surface of the sample can be reconstructed from the measured data. To scan the area of interest raster trajectories are employed, since this scan patterns are commonly applied in imaging systems. To follow the scan trajectory, feedback controllers are designed using the H_∞-approach. With the applied novel high performance compact FSM a closed loop bandwidth of 1.4 kHz is achieved. The measurement results show, that the calculated height of the rotational scan matches with the results of a classical mechanical scanning system. Therefore, it can be concluded that it is possible to manipulate only illumination path with a compact FSM and still satisfy the imaging condition.

ACKNOWLEDGEMENTS

REFERENCES

Blais, F., Rioux, M., and Beraldin, J.A. (1988). Practical considerations for a design of a high precision 3-d laser scanner system. *Optomechanical and electro-optical design of industrial systems*, 959, 225–247.

Brosed, F.J., Aguilar, J.J., Guilloma, D., and Santolaria, J. (2010). 3d geometrical inspection of complex geometry parts using a novel laser triangulation sensor and a robot. *Sensors*, 11(1), 90–110.

Csencsics, E., Schlarp, J., and Schitter, G. (2017). Bandwidth extension of hybrid-reluctance-force-based tip/tilt system by reduction of eddy currents. In *Proceedings of the 2017 IEEE International Conference on Advanced Intelligent Mechatronics (AIM2017)*, 1167–1172. IEEE.

Csencsics, E., Schlarp, J., Schopf, T., and Schitter, G. (2018). Compact high performance hybrid reluctance actuated fast steering mirror system. *IFAC Mechatronics*. Submitted.

Donges, A. and Noll, R. (2015). *Laser measurement technology.* Springer, Atlanta.

Goldstein, J.I., Newbury, D.E., Michael, J.R., Ritchie, N.W., Scott, J.H.J., and Joy, D.C. (2017). *Scanning electron microscopy and X-ray microanalysis.* Springer.

Hedding, L.R. (1990). Fast steering mirror design and performance for stabilization and single axis scanning. In *Acquisition, Tracking, and Pointing IV*, volume 1304, 14. International Society for Optics and Photonics.

Ito, S., Poik, M., Csencsics, E.K., Schlarp, J., and Schitter, G. (2018). Scanning chromatic confocal sensor for fast 3d surface characterization. In *Proceedings of the ASPE and EUSPEN Summer Topical Meeting, Advancing Precision in Additive Manufacturing*, 226–231.

Keferstein, C.P. and Dutschke, W. (2010). *Fertigungsmesstechnik.* Springer Vieweg, Wiesbaden.

Kunzmann, H., Pfeifer, T., Schmitt, R., Schwenke, H., and Weckenmann, A. (2005). Productive metrology - adding value to manufacture. *CIRP Annals-Manufacturing Technology*, 54(2), 155–168.

Kwakernaak, H. (1993). Robust control and h$_\infty$ optimization tutorial paper. *Automatica*, 29(2), 255–273.

Leach, R. (2011). *Optical measurement of surface topography*, volume 14. Springer, Berlin Heidelberg.

Leopold, J., Günther, H., and Leopold, R. (2003). New developments in fast 3d-surface quality control. *Measurement*, 33(2), 179–187.

Pfeifer, T. (2013). *Koordinatenmeßtechnik für die Qualitätssicherung: Grundlagen-Technologien-Anwendungen-Erfahrungen.* Springer-Verlag.

Schitter, G., Scarpas, A., and Allgöwer, F. (2004). Robust two-degree-of-freedom control of an atomic force microscope. *Asian Journal of Control*, 6(2), 156–163.

Schitter, G. and Stemmer, A. (2004). Identification and open-loop tracking control of a piezoelectric tube scanner for high-speed scanning probe microscopy. *IEEE Transactions on Control Systems Technology*, 12(3), 449–454.

Schlarp, J., Csencsics, E., and Schitter, G. (2018a). Feature detection and scan area selection for 3d laser scanning sensors. In *Proceedings of the 2018 IEEE/ASME International Conference on Advanced Intelligent Mechatronics (AIM 2018)*, 280–285. IEEE.

Schlarp, J., Csencsics, E., and Schitter, G. (2018b). Influence of scheimpflug condition on measurements of a scanning laser line sensor for 3d imaging. *Journal of Physics: Conference Series*, 1065(14), 142006.

Schlarp, J., Csencsics, E., and Schitter, G. (2018c). Optical scanning of a laser triangulation sensor for 3d imaging. *IEEE Transactions on Instrumentation and Measurement.* Submitted.

Schlarp, J., Csencsics, E., and Schitter, G. (2018d). Optical scanning of laser line sensors for 3D imaging. *Applied Optics*, 57(18), 5242–5248.

Schlarp, J., Csencsics, E., and Schitter, G. (2019). Sensoranordnung und Verfahren zum Vermessen eines Messobjekts. Deutsches Patent- und Markenamt 102019200664.7.

Schmitt, R. and Moenning, F. (2006). Ensure success with inline-metrology. In *XVIII IMEKO world congress Metrology for a Sustainable Development*, 235.1–235.6.

Schwenke, H., Neuschaefer-Rube, U., Pfeifer, T., and Kunzmann, H. (2002). Optical methods for dimensional metrology in production engineering. *CIRP Annals-Manufacturing Technology*, 51(2), 685–699.

Weckenmann, A., Estler, T., Peggs, G., and McMurtry, D. (2004). Probing systems in dimensional metrology. *CIRP Annals-Manufacturing Technology*, 53(2), 657–684.

Yu, C., Chen, X., and Xi, J. (2017). Modeling and calibration of a novel one-mirror galvanometric laser scanner. *Sensors*, 17(1), 164.